

# Defect Perovskites under Pressure: Structural Evolution of $\text{Cs}_2\text{SnX}_6$ ( $\text{X} = \text{Cl}, \text{Br}, \text{I}$ )

Giannis Bounos,<sup>†,‡</sup> Maria Karnachoriti,<sup>‡,‡</sup> Athanassios G. Kontos,<sup>\*,†,‡,§</sup> Constantin C. Stoumpos,<sup>§,||</sup> Leonidas Tsetseris,<sup>‡</sup> Andreas Kaltzoglou,<sup>†,||</sup> Xiaofeng Guo,<sup>||</sup> Xujie Lü,<sup>⊥</sup> Yannis S. Raptis,<sup>‡</sup> Mercouri G. Kanatzidis,<sup>§,||</sup> and Polycarpos Falaras<sup>†,||</sup>

HPSTAR  
662-2018

<sup>†</sup>Institute of Nanoscience and Nanotechnology, National Center for Scientific Research “Demokritos”, Agia Paraskevi Attikis, 15341 Athens, Greece

<sup>‡</sup>Department of Physics, National Technical University of Athens, 15780 Athens, Greece

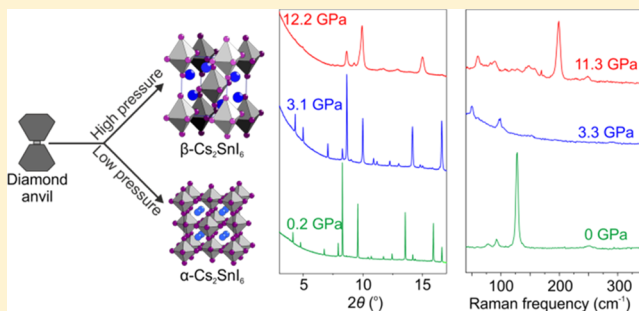
<sup>§</sup>Department of Chemistry, Northwestern University, Evanston, Illinois 60208, United States

<sup>||</sup>Department of Chemistry and Alexandra Navrotsky Institute for Experimental Thermodynamics, Washington State University, Pullman, Washington 99164, United States

<sup>⊥</sup>Center for High Pressure Science and Technology Advanced Research, Shanghai 201203, China

## Supporting Information

**ABSTRACT:** The application of pressure on halide perovskite materials provides key insights into their structural properties and the collective motions of their basic structural units. Here, we use synchrotron X-ray diffraction and Raman spectroscopy measurements combined with density functional theory calculations to perform a comprehensive study on the structural and vibrational properties of the so-called defect halide perovskites  $\text{Cs}_2\text{SnX}_6$  ( $\text{X} = \text{Cl}, \text{Br}, \text{I}$ ) under high hydrostatic pressures up to 20 GPa. We find that, while  $\text{Cs}_2\text{SnCl}_6$  and  $\text{Cs}_2\text{SnBr}_6$  retain a face-centered cubic (FCC) structure for all studied pressures,  $\text{Cs}_2\text{SnI}_6$  undergoes successive phase transformations initially to a more disordered structure and secondly to a low-symmetry monoclinic  $I2/m$  phase. The first transition is only evidenced by certain features emerging in the Raman spectra at  $\sim 3.3$  GPa, whereas the latter happens in a pressure window of around 8–10 GPa and involves tilting and elongation of  $\text{SnI}_6$  octahedra and hysteretic behavior with pressure release. Overall, the results reveal that pressure can alter significantly the structural characteristics of certain defect perovskites, such as  $\text{Cs}_2\text{SnI}_6$ , which is also anticipated to affect their optoelectronic properties.



## 1. INTRODUCTION

Perovskite halides have proven to be excellent light absorbers in solar cells and have revolutionized the field of third-generation photovoltaics.<sup>1,2</sup> The champion perovskite materials leading to maximum power conversion efficiencies are the three-dimensional (3D) hybrid lead iodide compounds containing methylammonium (MA:  $\text{CH}_3\text{NH}_3$ ),  $\text{MAPbI}_3$ , and formamidinium (FA:  $\text{NH}_2\text{CH}=\text{NH}_2$ ),  $\text{FAPbI}_3$ , which have energy gaps near the optimum Shockley–Queisser limit (1.34 eV). A key challenge for the exploitation of halide perovskites for industrial applications is the replacement of the toxic Pb by Sn. However, the stability of 3D tin perovskite halide analogues is poor due to the spontaneous oxidation of  $\text{Sn}^{2+}$  to  $\text{Sn}^{4+}$ .

$\text{Cs}_2\text{SnX}_6$  ( $\text{X} = \text{Cl}, \text{Br}, \text{I}$ ) crystallize into the vacancy-ordered double-perovskite structure (space group  $Fm\bar{3}m$ ).<sup>4–6</sup> They can be regarded as a zero-dimensional defect variant of the simple 3D perovskite  $\text{CsSnI}_3$  structure with isolated  $[\text{SnI}_6]^{2-}$  octahedra. Despite the absence of 3D covalency via  $\text{Sn}-\text{X}-$

$\text{Sn}$  connectivity, the close-packed anionic lattice forms dispersive frontier electronic bands with mobile carriers, which are activated by intrinsic defects in the structure, most probably iodine vacancies.<sup>7</sup> Combined with the advantage of the nontoxicity of Sn and their very high stability in oxygen and moisture,<sup>4,8</sup> the defect perovskites are very interesting materials in photovoltaics, both as light absorbers<sup>9</sup> and as hole-transporting materials.<sup>10–12</sup> Furthermore, changing the halide species affects dramatically the band gap, going from 1.26 eV for  $\text{Cs}_2\text{SnI}_6$  up to 3.9 eV for  $\text{Cs}_2\text{SnCl}_6$ .<sup>10</sup>

Pressure on the giga-pascal (GPa) scale can be used as an external stimulus to investigate the behavior of perovskite absorbers in a controllable and predictable way, since it is known to trigger a wide variety of structural transformations in organic and inorganic solids.<sup>13</sup> Apart from the structural

Received: August 30, 2018

Revised: October 1, 2018

Published: October 3, 2018

changes, the influence of high pressure on the perovskite optical and electronic transport properties,<sup>14–17</sup> including the observation of intense piezochromism,<sup>15,18</sup> have been investigated. In particular, understanding the correlations between pressure-induced structural and electronic changes allows us to tune more precisely material properties through compression.<sup>19</sup> In MAPbCl<sub>3</sub>, applied pressures above 0.8 GPa strongly affect the rocking vibration of the MA cation, which is confined by the surrounding PbCl<sub>6</sub> octahedra.<sup>17</sup> Tilting and distortion of the octahedra occur above 1.9 GPa lowers the symmetry and induces large changes in the Raman spectra. Comparative pressure X-ray diffraction (XRD) and Raman experiments on FAPbBr<sub>3</sub> and MAPbBr<sub>3</sub><sup>14</sup> show progressive phase transition from *Pm* $\bar{3}$ *m* to *Im* $\bar{3}$  and *Pnma*. The critical pressures of phase transitions are higher for FAPbBr<sub>3</sub> because of the less compressible character of its formamidinium cation. Extensive high-pressure XRD and photoluminescence studies have also been performed on MAPbI<sub>3</sub>.<sup>20</sup> The ambient-pressure tetragonal polymorph transforms first to a CoAs<sub>3</sub>-type cubic phase at 0.3 GPa and then to an orthorhombic phase above 2.7 GPa. This is accompanied by initial reduction and then increase of the band gap above critical pressures.

Hybrid MASnI<sub>3</sub>, FASnI<sub>3</sub>, and MA<sub>0.5</sub>FA<sub>0.5</sub>SnI<sub>3</sub> are among the most compressible known perovskites (overall bulk moduli *B*<sub>0</sub> are 12.6(7), 8.0(7), and 11.5(7) GPa, respectively).<sup>21</sup> Upon applying hydrostatic pressure, first, a CoAs<sub>3</sub>-type doubling of the primitive cubic unit cell occurs, resulting from octahedral tilting, followed by a symmetry lowering and an eventual amorphization above 4 GPa. Differences between the pristine and the pressure-treated MASnI<sub>3</sub> up to 30 GPa have been studied by synchrotron XRD (SXRD) and Raman spectroscopy.<sup>22</sup> A phase transition from tetragonal to orthorhombic at 0.7 GPa was observed, followed by an amorphization starting at about 3 GPa. Interestingly, no amorphization was observed during the recompression process, exhibiting a significant dependence on the compression history. The crystalline phase of the pressure-treated MASnI<sub>3</sub> persists to at least 30 GPa, showing improved structural stability, electrical conductivity, and visible light photoresponse.

The defect halide perovskites possess diverse crystallographic phases according to the size of the cations and the anions<sup>23</sup> and a rich phase diagram in temperature and pressure space. Early studies have shown that, upon cooling, they undergo cooperative octahedral tilting and rotations in symmetry-lowering phase transitions.<sup>24–27</sup> In the past,<sup>28</sup> some A<sub>2</sub>MCl<sub>6</sub> defect perovskites (A = Cs, Rb, K and M = Sn, Te, Pt) were systematically examined, including K<sub>2</sub>SnCl<sub>6</sub> and [(CH<sub>3</sub>)<sub>4</sub>N]<sub>2</sub>SnCl<sub>6</sub>, which showed no phase changes but small anomalies in the frequency versus pressure curves at low pressures. Very recently, a combined XRD and Raman high pressure study on Cs<sub>2</sub>SnBr<sub>6</sub> has found no phase transformation up to 20 GPa, in agreement with our findings, which we will discuss in detail below.<sup>29</sup> Regarding Cs<sub>2</sub>SnI<sub>6</sub>, the most relevant study up to now is the pressure-dependent X-ray investigation of cubic Cs<sub>2</sub>PdI<sub>6</sub> and tetragonal Cs<sub>2</sub>PdI<sub>4</sub>I<sub>2</sub>.<sup>30,31</sup> The two systems are related by a solid-state electron-transfer reaction of Cs<sub>2</sub>PdI<sub>4</sub>I<sub>2</sub> to Cs<sub>2</sub>PdI<sub>6</sub> at pressures of 2 GPa, while above 8 GPa, a transition to a low-symmetry polymorph is observed, indexed to the *I2/m*, which is a subset of the monoclinic space group *C2/m* (Nr. 12). Upon cooling, Cs<sub>2</sub>SnI<sub>6</sub> does not show any phase transformation down to 10 K, in contrast to Rb<sub>2</sub>SnI<sub>6</sub>, which, due to the smaller Rb<sup>+</sup> ion relative to Cs<sup>+</sup>, transforms

from tetragonal to the *P2/m* monoclinic phase, expressed by cooperative octahedral tilting of the SnI<sub>6</sub> octahedra.<sup>32</sup>

The current work examines the effect of applying high pressures of up to 20 GPa on the crystal structure and the vibrational properties of the defect perovskites Cs<sub>2</sub>SnX<sub>6</sub> (X = Cl, Br, I). While the crystal structures of Cs<sub>2</sub>SnCl<sub>6</sub> and Cs<sub>2</sub>SnBr<sub>6</sub> remain intact under pressure, we find that Cs<sub>2</sub>SnI<sub>6</sub> is prone to disorder and phase transformations, something that could be explored in the future to tune its optical, electronic, and conducting properties.

## 2. EXPERIMENTAL SECTION

**2.1. Chemical Synthesis.** The Cs<sub>2</sub>SnX<sub>6</sub> (X = Cl, Br, I) perovskites were prepared from their binary precursors, as previously described.<sup>10</sup> The polycrystalline materials are stable in air and have distinct colors, black, yellow, and white for the I, Br, and Cl derivatives, respectively.

**2.2. High-Pressure Synchrotron X-ray Diffraction.** A symmetric diamond anvil cell (DAC) was employed to generate high pressure. A rhenium gasket was preindented to 30 μm in thickness followed by laser drilling a 150 μm diameter hole in the central part to serve as the sample chamber. Powdered Cs<sub>2</sub>SnX<sub>6</sub> (X = Br, I) samples and ruby microspheres (for pressure measurements) were loaded in the chamber. Silicone oil was used as the pressure-transmitting medium and the pressures were determined by the ruby fluorescence method.<sup>33</sup> The in situ high-pressure angle-dispersive X-ray diffraction experiments were carried out at B1 station, Cornell High Energy Synchrotron Source (CHESS), Cornell University. A monochromatic X-ray beam with the wavelength of λ = 0.4859(3) Å was used for the diffraction experiments. The diffraction data were recorded by a Mar345 detector, and the sample-to-detector distance and other detector sitting parameters were calibrated using the powder standard of CeO<sub>2</sub>. The raw two-dimensional images were integrated to one-dimensional (1D) patterns with the Fit2D program.<sup>34</sup> To determine the unit cell parameters, the XRD data were analyzed using the Le Bail method with the Jana2006 program.<sup>35</sup> The starting structural parameters of the cubic (*Fm* $\bar{3}$ *m*) phase were taken from a previous work.<sup>10</sup> We then used the refined structural parameters as the starting parameters for the next pressure and continued this procedure systematically with increasing pressure. The structural phase transition of Cs<sub>2</sub>SnI<sub>6</sub> was analyzed using the previously reported group-theoretical analysis for double perovskites.<sup>36</sup> For the case of α-Cs<sub>2</sub>SnI<sub>6</sub> at various pressures, full Rietveld refinements were carried out using the FULLPROF software.<sup>37</sup>

**2.3. Raman Measurements under Pressure.** Small pieces of defect perovskites in powder form, with crosswise dimensions 10–30 μm, were loaded into a Syassen–Holzapfel-type diamond anvil cell (DAC) along with bulk silicon (Si) or gallium phosphide (GaP) for monitoring the pressure.<sup>38</sup> A metal gasket with a central hole of ca. 150–250 μm in diameter was inserted between the two diamonds of the setup. Apart from the sample and the calibration unit, the gasket was filled with a 4:1 methanol–ethanol pressure-transmitting medium. The latter provides good hydrostatic conditions up to a pressure of 12 GPa (at which it solidifies) and quasi-hydrostatic ones above this pressure. These facts have been confirmed by the absence of significant broadening of the Raman spectra. Raman data were obtained up to 20 GPa in several experimental sessions with repeated cycles of increasing and decreasing the pressure. Overall, silicon calibration

material in combination with 250  $\mu\text{m}$  diameter holes in the gaskets were used for detailed characterization of the perovskites at low pressures of up to 7 GPa, and GaP in combination with the lowest 150  $\mu\text{m}$  diameter gaskets for recording the high-pressure data.

Room-temperature micro-Raman spectra were measured in backscattering configuration on a Renishaw inVia Reflex spectrometer using a high-power near-infrared diode laser ( $\lambda = 785 \text{ nm}$ ) as the excitation source. The laser beam was focused onto the samples on spots of 4  $\mu\text{m}$  in diameter by means of a  $\times 20$  magnification lens, with an extra-long working distance of 25 mm necessary to overcome the thickness of the DAC sapphire window and a numerical aperture of 0.25. The scattered beam was filtered at  $30 \text{ cm}^{-1}$  with a double Rayleigh dielectric filter and analyzed on a 250 mm focal length spectrometer along with a 1200 lines/mm diffraction grating and a high-sensitivity charge-coupled device detector. Initially, laser power tests were carried out and a power of 0.3 mW was determined to be safe enough to avoid laser-induced thermal shifts of the Raman bands. Furthermore, a large number of spectra acquired from different spots of each sample verified uniformity and circular polarization of incident beam was adopted to minimize intensity differences of the spectra lines from the spectral acquisition of different sample beads. Frequency shifts were systematically calibrated by an internal bulk Si reference.

**2.4. Computational Methods.** The results were obtained with the density functional theory (DFT) code Quantum Espresso.<sup>39</sup> We employed projector-augmented waves<sup>40,41</sup> to describe the interactions between valence electrons and ions and a generalized-gradient approximation exchange-correlation functional,<sup>42</sup> while van der Waals (vdW) interactions were included with the DFT-D2 method.<sup>43</sup> By setting the  $C_6$  vdW coefficients<sup>42</sup> of I, Sn, and Cs equal, respectively, to 250, 825, and 2500 in atomic units, we obtained a lattice parameter (11.62 Å) for  $\alpha\text{-Cs}_2\text{SnI}_6$ , which is in excellent agreement with the experimental value. With the same set of  $C_6$  coefficients, the calculated lattice parameter for  $\alpha\text{-CsSnI}_3$  differs by less than 0.3% from the experimental data.<sup>44,45</sup> The relaxation of atomic positions and unit cells was performed with an energy cutoff of 50 Rydbergs (Ry) for the plane-wave basis and was terminated when the energy converged within  $10^{-6}$  Ry. Sampling of reciprocal space employed the Mohnkhorst–Pack scheme<sup>46</sup> and a  $6 \times 6 \times 6$   $k$ -grid. Calculations with higher energy cutoffs and finer  $k$ -point meshes confirmed the convergence of the results on relative stability and lattice parameters.

### 3. RESULTS AND DISCUSSION

**3.1. Synchrotron X-ray Diffraction Analysis.** All materials are indexed at room pressure in the FCC cubic space group  $Fm\bar{3}m$ . Only a trace amount of CsI (strongest peak at  $2\theta = 8.6^\circ$ ) was detected for the  $\text{Cs}_2\text{SnI}_6$  sample. In the order of I, Br, and Cl derivatives, lattice constants are 11.6377(1), 10.8371(1), and 10.3817(1) Å and Sn–X bond lengths are at 2.855, 2.7520, and 2.4886 Å.  $\text{Cs}_2\text{SnX}_6$  perovskites are expected to have an enhanced compressibility and structural flexibility due to their large framework vacancies. In situ synchrotron X-ray diffraction (SXRD) measurements under high pressure for  $\text{Cs}_2\text{SnBr}_6$  and  $\text{Cs}_2\text{SnI}_6$  confirm this hypothesis (Figure 1).

Both compounds can be reversibly compressed up to approximately 16 GPa, returning to their original structure

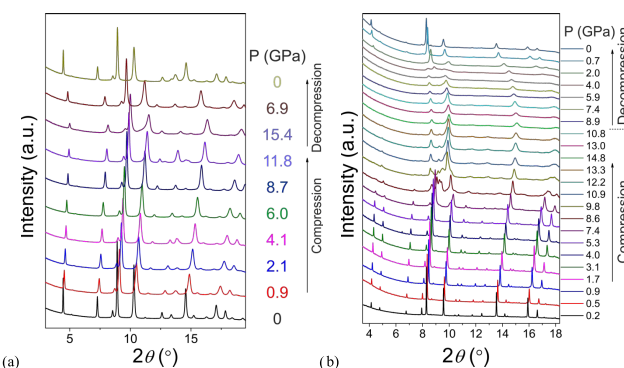


**Figure 1.** X-ray powder diffraction patterns ( $\lambda = 0.4859 \text{ \AA}$ ) under hydrostatic pressure for (a)  $\text{Cs}_2\text{SnBr}_6$ , where the FCC structure remains unchanged up to 15.4 GPa and (b)  $\text{Cs}_2\text{SnI}_6$ , which presents a drastic change upon compression above ca. 8–10 GPa, whereupon the FCC lattice changes to the monoclinic  $I2/m$ . This structure change is reversible with hysteresis, and the compound returns to its original FCC structure upon decompression below 4 GPa.

upon decompression. The cubic unit cell shrinks continuously with increasing pressure, expressed by the calculated bulk moduli of  $B_0 = 15.4 \text{ GPa}$  for  $\text{Cs}_2\text{SnI}_6$  and  $B_0 = 13.5 \text{ GPa}$  for  $\text{Cs}_2\text{SnBr}_6$ , estimated by means of the Birch–Murnaghan equation of states.<sup>47,48</sup> The pressure dependence of the  $V_0/V$  ratio (Figure 2) shows linear dependence in two regions, below

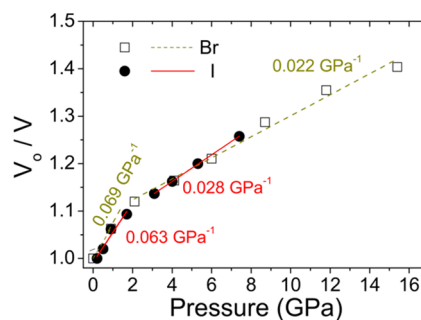


**Figure 2.** Pressure dependence of  $V_0/V$  for  $\text{Cs}_2\text{SnI}_6$  and  $\text{Cs}_2\text{SnBr}_6$  in their cubic phase. Linear fitting of the data below and above 2 GPa are shown. Gradient values correspond to the isothermal compressibility,  $\beta_T$ .

and above a pressure of ca. 2 GPa. The gradient which expresses the isothermal compressibility decreases from  $\beta_T = 0.063 \text{ GPa}^{-1}$  (below) to  $0.028 \text{ GPa}^{-1}$  (above 2.5 GPa) for  $\text{Cs}_2\text{SnI}_6$  and from  $\beta_T = 0.069$  to  $0.022 \text{ GPa}^{-1}$  for  $\text{Cs}_2\text{SnBr}_6$ .

The obtained bulk moduli indicated that the  $\text{Cs}_2\text{SnX}_6$  compounds possess characteristics of an extended lattice rather than molecular characteristics, as this is implied by the crystal structure comprising discrete  $[\text{SnX}_6]^{2-}$  octahedra and  $\text{Cs}^+$  ions in an FCC lattice. This statement is corroborated by the fact that the bulk moduli of  $\text{Cs}_2\text{SnX}_6$  are very similar to the extended hybrid perovskite  $\text{CH}_3\text{NH}_3\text{SnI}_3$  ( $B_0 = 12.3 \text{ GPa}$ ), which is a representative compound with a three-dimensional (3D) lattice,<sup>49</sup> rather than a molecular compound, such as  $\text{SnI}_4$  ( $B_0 = 5.2 \text{ GPa}$ ).<sup>50</sup>

$\text{Cs}_2\text{SnBr}_6$  retains its cubic crystal lattice within the studied pressure range in accordance with ref 29 with almost ideal reversible characteristics as shown by the SXRD patterns at all applied pressures (Figure 1a). The full width at half-maximum (FWHM) of the strongest (222) reflection presents good

reversibility in the pressure cycle (Figure S1a).  $\text{Cs}_2\text{SnI}_6$ , on the other hand, undergoes a continuous structural phase transition starting at  $\sim 8$  GPa and completing at  $\sim 10$  GPa, with both the original cubic phase and the transformed monoclinic phase being present between 8 and 10 GPa (Figure 1b). Furthermore, upon pressure release, the reverse phase transition to the ambient-pressure FCC structure is completed only below 4 GPa. The large increase in the FWHM values of the strongest (222) reflection suggests reduced crystallinity of the material upon pressure release (Figure S1b). According to the Rietveld analysis of the SXRD patterns, at low pressure (Figure S2a at 0.9 GPa),  $\text{Cs}_2\text{SnI}_6$  has the FCC structure ( $\alpha$ -phase) while at high pressure (see Figure S2b at 10.9 GPa), the material adopts a nearly orthogonal monoclinic  $I2/m$  structure, termed  $\beta$ - $\text{Cs}_2\text{SnI}_6$  based on phase transition nomenclature. In fact,  $I2/m$  is among the candidate structures often encountered in high-pressure distorted perovskites.<sup>36</sup> Another plausible one is the  $P4/mnc$  tetragonal phase, which partially fits the experimental SXRD reflections, too; however, this fit is clearly worse than that of the  $I2/m$  structure reported in Figure S2b. The phase transition to  $\beta$ - $\text{Cs}_2\text{SnI}_6$  occurs through tilting of the  $\text{SnI}_6$  octahedra about the monoclinic  $b$  axis, accompanied by their axial expansion along the  $c$  axis, as presented in Figure 3b.

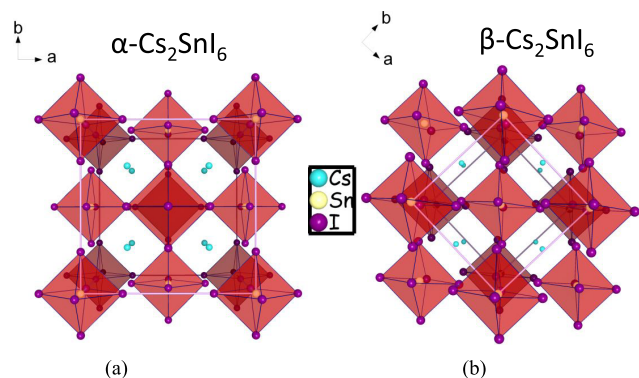


**Figure 3.** Crystal structure of  $\text{Cs}_2\text{SnI}_6$  (a) at ambient pressure (FCC  $\alpha$ -phase) that can be described with a body-centered tetragonal (BCT) unit cell and a lattice constant ratio  $c/a = \sqrt{2}$  and (b) at high pressure ( $I2/m$   $\beta$ -phase), which is derived from the BCT structure through tilting of the  $\text{SnI}_6$  octahedra about the  $b$  axis.

The lattice constants derived at 10.9 GPa are equal to  $a = 9.055$  Å,  $b = 7.396$  Å, and  $c = 8.644$  Å, and the crystallographic angle  $\beta$  is equal to  $94.24^\circ$ . The experimental refinement of the  $I2/m$  in terms of bond lengths or thermal displacements is not feasible because this is a monoclinic phase with many fitting parameters, which cannot be determined with accuracy due to the low diffraction intensity and the small number of resolved reflections (to some extent overlapping each other). Due to the absence of direct group–subgroup relationship between  $Fm\bar{3}m$  and  $I2/m$ , the corresponding phase transition under pressure for  $\text{Cs}_2\text{SnI}_6$  is of first order, confirmed also by the hysteresis in the reformation of the cubic phase upon releasing the pressure.

In contrast to the  $\beta$ -phase,  $\alpha$ - $\text{Cs}_2\text{SnI}_6$  is a cubic FCC structure with only few refinable parameters in the Rietveld analysis and significantly better signal-to-background ratio. The refinement in this case is feasible and permits, apart from the lattice parameters, the extraction of the inter- and intra-octahedral bond lengths. The deduced values at various pressures are shown in Table S1. As for the Sn–I bond lengths, they reach the lowest value of  $\sim 2.73$  Å under compression at 3.1 GPa, which is higher than the sum of the ionic radii<sup>51</sup> of the ions ( $0.69 + 2.20 = 2.89$  Å), suggesting significant covalency in the bonding and then the values remain almost constant regardless of further compression. A similar trend is found for the intra-octahedral I–I distances. As for the Cs–I bond lengths, they drop constantly under compression up to 7.4 GPa to 3.819 Å, which are much smaller than the sum of their ionic radii of the elements (ca. 4.4 Å). However, the inter-octahedral I–I distances, which mainly influence the band gap of defect perovskites,<sup>10</sup> are affected to a larger extent by compression, decreasing continuously from 4.1954 to 3.758 Å as a result of pressure-induced shrinkage of the lattice voids. Figure S3 presents graphically the average inter- and intra-octahedral I–I distances upon compression to 7.4 GPa. Apparently, at  $\sim 2$  GPa, the intra-octahedral I–I distance is reaching a threshold plateau being insensitive to further compression, while the inter-octahedral I–I bond length continues to decrease. These results denote a prestage of the tilting and deformation of the octahedra, which takes place at higher pressure in order that the atoms will be able to occupy space more efficiently. Qualitatively, this analysis confirms the empirical predictions<sup>23</sup> that the iodide derivative in the  $\text{Cs}_2\text{SnX}_6$  series is the only one vulnerable to phase changes

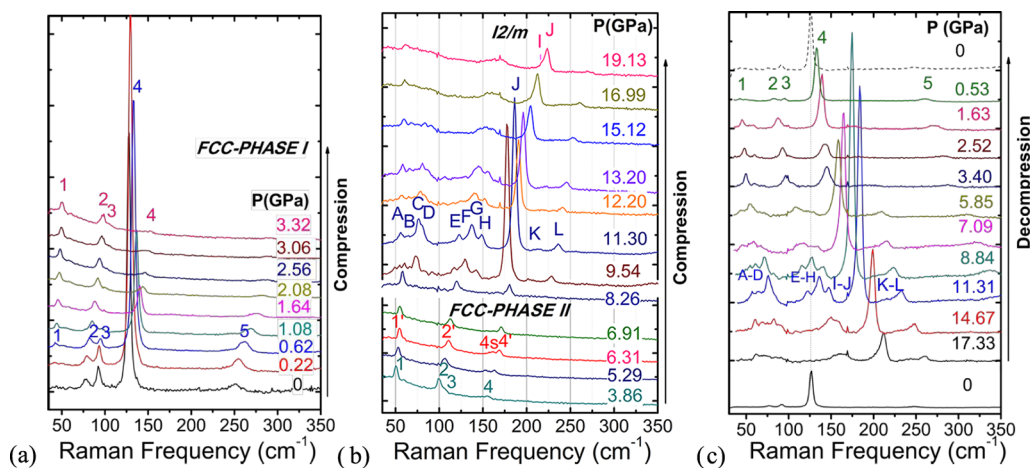


**Figure 4.** Selected Raman spectra of  $\text{Cs}_2\text{SnI}_6$  upon increasing the pressure (a) up to 3.3 GPa, (b) from 3.3 to 19.1 GPa, and (c) upon pressure release from 17.33 GPa to ambient pressure.

induced by pressure due to its low radius ratio defined as ratio of the radius of the Cs cation to the size of the cavity formed by the neighboring iodine anions.

**3.2. Raman Scattering Analysis.** The spectra of  $\text{Cs}_2\text{SnI}_6$  present very interesting changes upon increasing the pressure. To follow these changes, three sets of data are shown in this work. Detailed Raman spectra from ambient pressure up to 3.5 GPa are shown in Figure 4a and selected ones, above 3.5 GPa and up to 19 GPa, in Figure 4b. All Raman bands shift positively with pressure, as it is normally expected due to hardening of chemical bonding during compression. At ambient and very low pressure (0.22 GPa), only three first-order Raman bands are observed, all pertaining to Sn–I vibrations in the  $\text{SnI}_6$  octahedra: the triply degenerate asymmetric bending X–Sn–X deformation,  $\delta(\text{F}_{2g})$ , at  $78\text{ cm}^{-1}$  (mode #2), the doubly degenerate asymmetric Sn–X stretching  $\nu(\text{E}_g)$ , at  $92\text{ cm}^{-1}$  (mode #3), and the non-degenerate Sn–X symmetric stretching vibration,  $\nu(\text{A}_{1g})$ , at  $126\text{ cm}^{-1}$  (mode #4).<sup>10</sup> The latter is very strong with intensity 15 times larger than #3, which is the second more intense mode. The spectrum further includes the second order  $2\nu(\text{A}_{1g})$  mode at  $250\text{ cm}^{-1}$  (mode #5). Above 0.62 GPa, the missing triply degenerate lattice mode  $\nu_L(\text{F}_{2g})$  (mode #1), involving vibrations of the Cs atoms in the rigid  $[\text{SnI}_6]$  lattice, emerges at low frequency.<sup>10</sup> Extrapolation of the Raman shifts of this mode at zero pressure gives a value of  $41\text{ cm}^{-1}$  that corresponds to the frequency of the unobserved lattice mode at ambient pressure. By increasing the pressure up to about 3 GPa, apart from frequency shifts, we observe intensity changes of the #3 and #4 stretching modes (Figure S4). First, an intensity increase is observed, for mode #4 mode, up to 0.22 GPa, followed by gradual intensity decrease for both modes #3 and #4. Thus, at 3.3 GPa, mode #3 vanishes and mode #4 appears just above the detection threshold (Figure 4a) and this pattern continues up to 8 GPa. In this range (2–8 GPa), a new weak satellite band (we call it 4s) appears next to mode #4. Another interesting observation is that in the full range of the gradual phase transition, a strong elastic scattering background is established, which maximizes at 3.3 GPa. In Figure 5, we plot the frequencies of bands #1, #2, #3, #4, and #4s as a function of pressure (#1, #2 and #4 turn to #1', #2' and #4' above 3.3

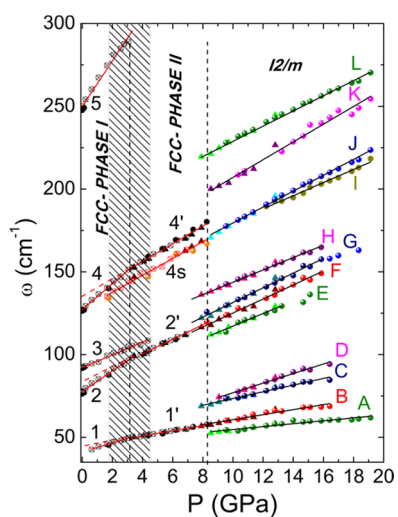


**Figure 5.** Pressure dependence of the Raman band frequencies of  $\text{Cs}_2\text{SnI}_6$  upon compression.

GPa). The aforementioned changes in the spectral characteristics, namely, dramatic decrease in the intensity of modes #3 and #4, the emergence of the mode #4s, and the enhancement of the elastic background suggest an order–disorder phase transition in the pressure range of about 3.3 GPa. This transition evolves gradually from 1.8 to 4.2 GPa. This is supported by a decrease in the slopes of the frequencies versus pressure for all modes, at about 3.3 GPa, which probably stems from the considerable reduction in the compressibility of the crystal. To make a comparison with the SXR D results, a full list of frequency shift versus pressure slopes ( $d\omega/dP$ ) and reduced slopes ( $\omega_0^{-1} [d\omega/dP]$ ) is given in Table 1, recording values below (phase I) and above (phase II) the 3.3 GPa. Indeed, the  $\sim 52\%$  reduction in the  $\omega_0^{-1} [d\omega/dP]$  slope of mode #1, which adsorbs the major part of the crystal compression, corresponds quite well to the  $\sim 44\%$  decrease of the compressibility determined in the XRD data.

The transformation from phase I to phase II has the characteristics of breaking the long-range translational symmetry of the lattice, introducing local disorder, reducing the empty spaces in the lattice, and making, thus, the crystal less compressible. Raman spectroscopy is very sensitive to such changes; SXR D, on the other hand, does show the change in compressibility, but it cannot detect new motifs in the SXR D patterns or abrupt changes in the FWHM of the peaks because the average long-range order apparently is hardly affected.<sup>32</sup> Thus, for SXR D, phase II is indistinguishable to the ambient-pressure  $Fm\bar{3}m$  one, while Raman data detect it as a new intermediate phase between 3 and 8 GPa. Such discrepancies in the phase identification between SXR D and Raman measurements close to order/disorder phase transitions often appear in the literature.<sup>52</sup> This transition from phase I to phase II resembles that induced by reduction of the temperature in the isostructural  $\text{K}_2\text{SnCl}_6$ .<sup>53</sup> It is accompanied by the weakening of the symmetric Sn–I stretching mode #4 and the emergence of the new mode #4s with lower frequency but identical frequency versus pressure slope, which indicates that it also originates from Sn–I stretching, albeit at a bigger Sn–I distance, which can be taken as a signal of metastability toward a phase with monoclinic symmetry. Moreover, the emergence of a strong quasi-elastic scattering spectral continuum is a characteristic feature of relaxational dynamics. This type of elastic background is observed only in the high-temperature cubic and tetragonal phase of  $\text{CsPbBr}_3$  and  $\text{MAPbBr}_3$  (not in the low-temperature orthorhombic phase) and is attributed to local polar fluctuations in the structure.<sup>54</sup> A similar analysis on our data shows enhancement of the central quasi-elastic continuum exactly at the critical pressure (3.3 GPa) of the phase transition, suggesting increased anharmonic/disordered motion. From the width of the corresponding central broad scattering band  $\Gamma = 165\text{ cm}^{-1}$ , a Debye relaxation time  $\tau_r$  of the order of 32 fs is estimated, according to the formula  $\tau_r = 1/2\pi c\Gamma$ .

Above 8–10 GPa, an abrupt change, consistent with the changes in the X-ray diffraction patterns described above is observed in the Raman spectra. Twelve modes have been resolved named as A–L. Shifts versus pressure are shown in Table S2. A small decline of the shift versus pressure gradients above 13 GPa is attributed to the relaxation of the pure hydrostatic conditions of the pressure medium.

Accordingly, we compared the 12 modes identified in the Raman spectra above 8 GPa with those predicted by the group theory for the  $I2/m$  space group, which was indexed in the

**Table 1.** Values of Zero-Pressure Raman Frequencies ( $\omega_0$ ), Frequency Shift vs Pressure Slopes ( $d\omega/dP$ ), Reduced Slopes ( $\omega_0^{-1} [d\omega/dP]$ ) of  $\text{Cs}_2\text{SnI}_6$  in the FCC-Phase I and II<sup>a</sup>

	peak	$\omega_{p-T}(\text{cm}^{-1})$	$\omega_0(\text{cm}^{-1})$	$d\omega/dP(\text{cm}^{-1}/\text{GPa})$	$\omega_0^{-1}(d\omega/dP \cdot 10^{-3} \text{ GPa}^{-1})$	$\gamma$
PHASE I $\approx 0\text{--}3.3$ GPa	1		$41.1 \pm 0.3$	$2.79 \pm 0.14$	67.9	1.08
	2		$77.7 \pm 0.3$	$6.24 \pm 0.16$	80.3	1.27
	3		$92.2 \pm 0.3$	$3.84 \pm 0.11$	41.6	0.66
	4		$127.1 \pm 0.3$	$7.86 \pm 0.18$	61.8	0.98
	5		$250.0 \pm 0.8$	$13.72 \pm 0.46$	54.9	
PHASE II $\approx 3.3\text{--}8.0$ GPa	1'	50.1	$44.5 \pm 0.3$	$1.58 \pm 0.06$	35.5	
	2'	99.8	$83.0 \pm 0.7$	$4.38 \pm 0.12$	52.8	
	4'	152.8	$134.9 \pm 0.8$	$5.36 \pm 0.14$	39.7	
	4s	135.2	$127.5 \pm 0.9$	$5.09 \pm 0.16$	39.9	

<sup>a</sup>Grüneisen parameters ( $\gamma$ ) in phase I and frequencies at the critical pressure of 3.3 GPa, where phase transformation occurs ( $\omega_{p-T}$ ) in phase II, are also given.

XRD analysis as the high-pressure phase and they were found in full agreement. This particular group has a total of  $9 \times 3 = 27$  expected normal modes with  $k = 0$ , which are theoretically divided into the following one-dimensional ( $A_{g(u)}$ ,  $B_{g(u)}$ ) symmetry species of the  $C_{2h}$  point group.<sup>55</sup>

$$\Gamma_{27} = 7A_g + 6A_u + 5B_g + 9B_u$$

Of the above modes, all of the even-parity ones ( $g$ ) are summarized in 12 Raman-active ones ( $7A_g + 5B_g$ ), which are further divided in external, ( $2A_g + B_g$ ) due to vibrations of the Cs atoms against the octahedra and internal (all of the others), due to vibrations of the I atoms in the  $\text{SnI}_6$  octahedra.

From the Raman spectra recorded upon releasing the pressure, baseline-corrected and shown in Figure 4c, we observe that the phase transition from the low-symmetry  $I2/m$  phase to the cubic FCC occurs below 5.85 GPa (and above 3.3 GPa) upon releasing the pressure versus 8–10 GPa, which is the corresponding critical pressure for the phase transition in the increasing pressure experiments. Apparently, the spectrum at 5.85 GPa at reverse pressure scan resembles very well the characteristics of the spectra of the  $I2/m$  phase with the unambiguous observation of the intense J and the characteristic high-frequency L phonon bands. Therefore, a hysteresis of 2–5 GPa is observed in the phase transformation, in accordance with the SXRD results. The hysteresis in the transition to the original FCC structure upon releasing the pressure is visualized in the Raman frequency versus pressure graph of Figure S5, which includes data upon pressure increase and release marked with different symbols.

Variable-pressure Raman spectra obtained from the  $\text{Cs}_2\text{SnBr}_6$  and  $\text{Cs}_2\text{SnCl}_6$  perovskites, up to about 12 GPa, are shown in Figures 6a and 7a, respectively. Their analysis is given in Figures 6b and 7b. A linear shift of the Raman bands with pressure is evidenced, without observing any peculiar features as those observed in the case of  $\text{Cs}_2\text{SnI}_6$ . The only exception is the low-frequency lattice mode #1 in  $\text{Cs}_2\text{SnCl}_6$ , which has a large frequency slope versus pressure, equal to  $5.4 \text{ cm}^{-1} \text{ GPa}^{-1}$ , up to 2 GPa, decreasing, for higher pressures to  $1.7 \text{ cm}^{-1} \text{ GPa}^{-1}$ . In contrast, the mode is not resolved below 2 GPa in the case of  $\text{Cs}_2\text{SnBr}_6$ . The intensities of all other Raman bands, including the stretching Sn–X ones are unaffected by the pressure and no extra modes or splitting is observed. Furthermore, for  $\text{Cs}_2\text{SnBr}_6$ , the frequency merging of the two modes #2 and #3, at pressures  $\geq 11$  GPa, is combined with a marginal change in the frequency slope versus pressure, for mode #4. It is not clear whether this is dynamically correlated

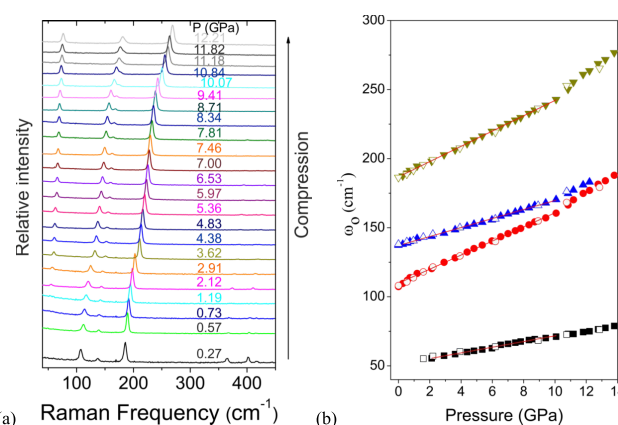


**Figure 6.** (a) Selected Raman spectra of  $\text{Cs}_2\text{SnBr}_6$  at elevated pressures. (b) Pressure dependencies of the Raman band frequencies of  $\text{Cs}_2\text{SnBr}_6$ . Open symbols correspond to the data analysis upon pressure release.

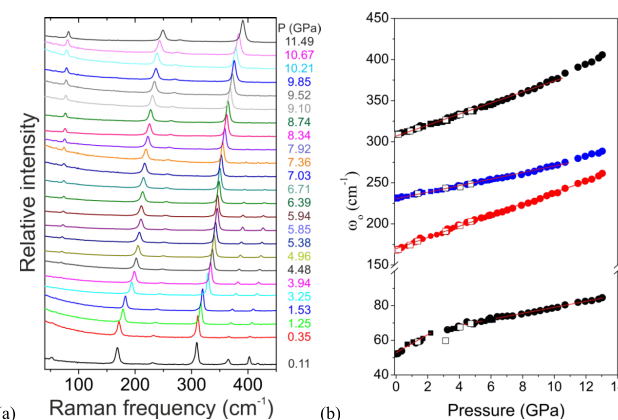


**Figure 7.** (a) Selected Raman spectra of  $\text{Cs}_2\text{SnCl}_6$  at elevated pressures. (b) Pressure dependencies of the Raman band frequencies of  $\text{Cs}_2\text{SnCl}_6$ . Open symbols correspond to the data analysis upon pressure release.

or a spontaneous coincidence. The only sign in the Raman spectra that is reminiscent of the behavior of  $\text{Cs}_2\text{SnI}_6$  is an increase of the elastic background up to about 1.5 GPa for both Br and Cl derivatives, but the effect is now very weak. Raman shifts versus pressure slopes are given in Table 2. The unresolved mode #1 at ambient pressure for  $\text{Cs}_2\text{SnBr}_6$  is predicted at  $51 \text{ cm}^{-1}$ , which is nearly identical to the frequency

**Table 2.** Values of Zero-Pressure Frequencies, Frequency Shift vs Pressure Slopes, Reduced Frequency Slopes, and Gruneissen Parameters for  $\text{Cs}_2\text{SnX}_6$  ( $X = \text{Br}$  and  $\text{Cl}$ )

peak	$\text{Cs}_2\text{SnBr}_6$				$\text{Cs}_2\text{SnCl}_6$			
	$\omega_0$ ( $\text{cm}^{-1}$ )	$d\omega/dP$ ( $\text{cm}^{-1} \text{GPa}^{-1}$ )	$\omega_0^{-1} [d\omega/dP]$ ( $\times 10^{-3} \text{GPa}^{-1}$ )	$\gamma$	$\omega_0$ ( $\text{cm}^{-1}$ )	$d\omega/dP$ ( $\text{cm}^{-1} \text{GPa}^{-1}$ )	$\omega_0^{-1} [d\omega/dP]$ ( $\times 10^{-3} \text{GPa}^{-1}$ )	$\gamma^b$
1	$51.1 \pm 0.3$	$2.06 \pm 0.05$	39.5	0.57	$52.2 \pm 0.5$ $60.9 \pm 0.3^a$	$5.4 \pm 0.4$ $1.73 \pm 0.04^a$	103.1 29.6 <sup>a</sup>	2.40 0.70 <sup>a</sup>
2	$109.8 \pm 0.3$	$5.10 \pm 0.05$	46.4	0.67	$169.6 \pm 0.3$	$6.85 \pm 0.05$	40.4	0.96
3	$137.1 \pm 0.3$	$3.26 \pm 0.04$	23.8	0.34	$229.8 \pm 0.4$	$4.19 \pm 0.10$	18.2	0.43
4	$186.8 \pm 0.3$	$5.54 \pm 0.02$	29.7	0.43	$307.1 \pm 0.7$	$6.60 \pm 0.08$	23.3	0.55

<sup>a</sup>Values for pressures above 2.0 GPa. <sup>b</sup>Values obtained with  $\beta_T = 0.042 \text{GPa}^{-1}$  taken from theoretical calculations.<sup>56</sup>

for  $\text{Cs}_2\text{SnCl}_6$  ( $52 \text{cm}^{-1}$ ), obtained directly from the spectra at  $P = 1$  bar. However, the extrapolation to  $P = 0$  of the  $\text{Cs}_2\text{SnCl}_6$  frequency data obtained for pressures above 2 GPa gives a fitting parameter of  $60.9 \text{cm}^{-1}$ . Figure S6 includes Raman spectra of  $\text{Cs}_2\text{SnBr}_6$  and  $\text{Cs}_2\text{SnCl}_6$  upon releasing the pressure, showing good spectral reversibility.

Apart from the values of  $\omega_0$  and the slopes  $d\omega/dP$ , Tables 1 and 2 further include calculated reduced slopes  $\omega_0^{-1} [d\omega/dP]$  and the Gruneissen parameters  $\gamma$  for each mode, estimated by the following relation

$$\gamma_i = -\left(\frac{\partial \ln \omega_i}{\partial \ln V}\right)_T = \frac{1}{\beta_T \omega_i} \left(\frac{\partial \omega_i}{\partial P}\right)_T$$

where we recall that  $\beta_T$  is the isothermal compressibility.

The results of the reduced slopes for the four Raman bands observed in all FCC structures are shown in Figure 8. We

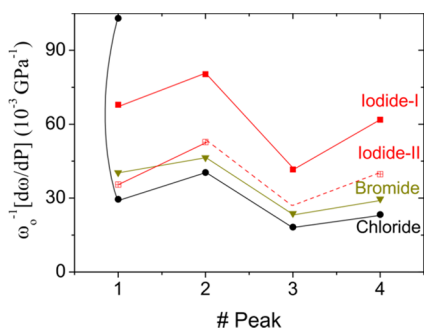


**Figure 8.** Reduced slopes  $\omega_0^{-1} [d\omega/dP]$  of the four first-order Raman bands in  $\text{Cs}_2\text{SnX}_6$  ( $X = \text{Cl}, \text{Br}, \text{I}$ ). For the iodide derivative, two sets of results are shown, for the initial phase I up to 3.3 GPa (red solid symbols) and the intermediate phase II at 3.3–8 GPa (red open symbols). In this second phase, the predicted value for the missing mode #3 is displayed. Lattice mode #1 for  $\text{Cs}_2\text{SnCl}_6$  initially shows very high reduced slope  $\approx 103 \times 10^{-3} \text{GPa}^{-1}$ , which drops to  $\approx 30 \times 10^{-3} \text{GPa}^{-1}$ , above 2 GPa.

chose to plot the reduced slopes versus mode number (rather than vs mode frequency) to display more clearly the systematic behavior with respect to the vibrational symmetry. For each compound, the set of attained reduced slopes stands at a different mean level, with considerable deviations between different bands, always maximum for mode #2 and minimum for mode #3. The trend of the mean reduced slope values is to increase in the order of  $\text{Cl} < \text{Br} < \text{I}$ . The initial values for  $\text{Cs}_2\text{SnI}_6$  in phase I are considerably higher than those of the Br and Cl derivatives. The reduced slopes decrease considerably in the intermediate phase II (by nearly 2 times for the lattice mode and 1.5 times for the Sn–I internal modes) at magnitudes analogous to those observed in the other systems.

For  $\text{Cs}_2\text{SnCl}_6$  and pressures up to 2 GPa, there is a very high value for the reduced slope of the lattice mode #1. Above 2 GPa, the value falls down to the standard expected level. Deduced values  $\gamma$  are near to unity in all cases, which is typical for covalent crystals.<sup>57</sup> The only exception is the initial (below 2 GPa) value for the Cl derivative, which reads  $\gamma = 2.4$  and suggests the strong ionic character of the Cs–Cl bond.

**3.3. Computational Results.** To explore the possibility of phase transitions of  $\text{Cs}_2\text{SnI}_6$  under pressure, we constructed a number of metastable  $\text{Cs}_2\text{SnI}_6$  structures. One set of such structures was created by removing Sn atoms from the  $\beta$ -,  $\gamma$ -, and Y-polymorphs of  $\text{CsSnI}_3$ .<sup>43,44</sup> Because all of the corresponding (relaxed)  $\text{Cs}_2\text{SnI}_6$  configurations are significantly less stable (by more than 0.3 eV per chemical formula) than FCC- $\text{Cs}_2\text{SnI}_6$ , they are not considered as good candidates for phase transitions, at least for the range of pressures considered in this work.

In the second set of trials, we applied various forms of tilts on the  $\text{SnI}_6$  octahedra. DFT calculations on the latter set identified overall the following four high-pressure phases: (i) monoclinic  $I2/m$  (Nr. 12a), (ii) monoclinic  $C2/m$  (Nr. 12b), (iii) tetragonal  $P4/mnc$  (Nr. 128), and (iv) tetragonal  $I4/m$  (Nr. 87). Phase Nr. 12b is practically the same with phase Nr. 87 and will thus not be discussed further below. Figure 9

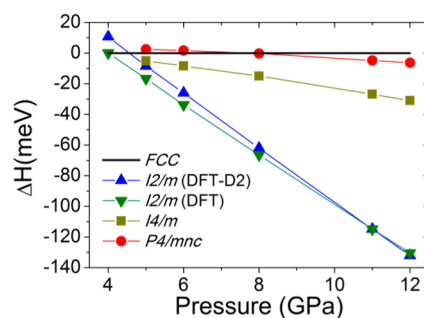


**Figure 9.** Calculated enthalpies (in meV per chemical formula) of the  $I2/m$ ,  $I4/m$ , and  $P4/mnc$   $\text{Cs}_2\text{SnI}_6$  polymorphs (referenced with respect to the FCC structure) as a function of pressure. The blue line corresponds to the  $I2/m$  case within the DFT-D2 approach. All other data are based on calculations without van der Waals interactions. Structures  $I4/m$  and  $P4/mnc$  are stabilized above 5 GPa.

presents the calculated enthalpies of the above-mentioned crystal phases as a function of pressure. As shown in the figure, above about 4.7 GPa, phase  $I2/m$  becomes the most stable among all structures, including the FCC ambient polymorph. When vdW interactions are included within the DFT-D2 approach, only the  $I2/m$  and FCC structures are stabilized, the  $I2/m$  phase above 2 GPa and the FCC structure at all pressures. In contrast, structures  $P4/mnc$  and  $I4/m$  relax

spontaneously to the FCC lattice. On the other hand, when vdW interactions are not included, structures  $P4/mnc$  and  $I4/m$  are also stabilized above 5 GPa.

The  $a$ ,  $b$ , and  $c$  lattice parameters of the  $I2/m$  structure at 2 GPa (this is the lowest pressure at which the  $I2/m$  polymorph exists as a metastable phase) are equal to 9.82, 8.04, and 8.97 Å, respectively, while the corresponding  $\alpha$ ,  $\beta$ , and  $\gamma$  angles of the cell are equal to 90, 92.8, and 90°. Figure 10 presents the

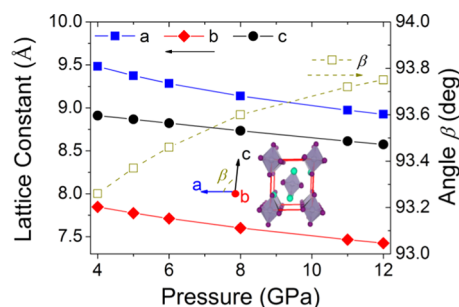


**Figure 10.** DFT results on the variation of the crystallographic parameters ( $a$ ,  $b$ , and  $c$  lattice constants and angle  $\beta$ ), in the  $\beta$ -phase ( $I2/m$ ) of  $Cs_2SnI_6$  as a function of applied pressure. The inset shows the conventional  $I2/m$  unit cell viewed along the  $b$  axis.

variation of the calculated lattice parameters and the crystallographic angle  $\beta$  as a function of pressure. The results are in very good agreement with the crystallographic data extracted from the SXRD experiments. In particular, the calculated (measured) values for the  $a$ ,  $b$ ,  $c$ , and  $\beta$  crystallographic parameters at 11 GPa (10.9 GPa) are equal, respectively, to 8.973 Å (9.055 Å), 7.466 Å (7.396 Å), 8.612 Å (8.644 Å), and 93.72° (94.24°). Figure S7 shows the distances between Sn atoms and their equatorial (Sn–I1 black line) and axial (Sn–I2 red line) iodine (I) neighbors. Furthermore, DFT calculations succeed with the prediction of a metastable phase transition at a relatively low pressure, about 2.0 GPa, which might be related to the order–disorder transition observed in Raman at 1.8–4.2 GPa, involving remote arrangement of some iodines at large Sn–I distances as well as the first-order transition to a low-symmetry phase at pressures above 4.7 GPa. Although this critical pressure differs considerably from the 8–10 GPa recorded in the SXRD and Raman experiments, it matches satisfactorily with the reverse  $I2/m$  to FCC transition, which occurs upon pressure release.

On the basis of the above findings on  $Cs_2SnI_6$ , we investigated whether  $Cs_2SnBr_6$  and  $Cs_2SnCl_6$  could undergo similar transitions under pressure between analogous  $\alpha$ - and  $\beta$ -phases. DFT-D2 calculations on the  $\alpha$ - (i.e., FCC) polymorphs of  $Cs_2SnBr_6$  and  $Cs_2SnCl_6$  (with the  $C_6$  coefficients<sup>42</sup> of Cs, Sn, Br, and Cl set to, respectively, 2500, 825, 108, and 44 in atomic units) give lattice constants in excellent agreement with experiments. In particular, the calculated lattice parameter of  $Cs_2SnBr_6$  ( $Cs_2SnCl_6$ ) is 10.86 Å (10.39 Å), whereas the experimental value<sup>58</sup> is 10.77 Å (10.36 Å). As for the  $\beta$ -phase, it exists as a metastable structure for both  $Cs_2SnBr_6$  and  $Cs_2SnCl_6$  in the pressure range between 10 and 20 GPa.

However, the  $\beta$ -phases of  $Cs_2SnBr_6$  and  $Cs_2SnCl_6$  are significantly less stable than the FCC crystals. For example, the enthalpy difference ( $\Delta H$ ) between the  $\alpha$  and  $\beta$  structures of  $Cs_2SnBr_6$  at 10 GPa is 123 meV per chemical formula. In the case of  $Cs_2SnCl_6$ , this difference is even larger at 193 meV. Figure S8 summarizes the results on  $\Delta H$  for  $Cs_2SnBr_6$  and

$Cs_2SnCl_6$ . On the basis of the results, we can conclude that there is no phase transition between  $\alpha$ - and  $\beta$ -crystal structures of these compounds in full agreement with the XRD and Raman experimental results. In fact, it should be noted that at 8 GPa, a structure initially prepared as a  $\beta$ -polymorph of  $Cs_2SnCl_6$  relaxes spontaneously to the FCC lattice.

#### 4. CONCLUSIONS

The study of the  $Cs_2SnX_6$  defect perovskites under hydrostatic pressure up to 20 GPa revealed a strong response on the materials' structural and vibrational properties. The most interesting results were obtained for the  $Cs_2SnI_6$  crystal, which shows a slow establishment of Raman characteristics at about 3.3 GPa, such as vanishing of the strongest Sn–I symmetric and asymmetric stretching modes, emergence of a new weak Raman band, next to the weak Sn–I symmetric band with similar pressure-induced shifts, strong reduction of the frequency versus pressure slopes, and maximization of the quasi-elastic background. This behavior consistently marks a gradual phase transition to a disordered state that is only evidenced in SXRD by reduction in the compressibility of the crystal. Above 8 GPa, a complete transformation of the thrifty to a multicomponent Raman spectrum marks the transition to a low-symmetry phase. This phase transformation was determined on the basis of synchrotron X-ray diffraction as the monoclinic  $I2/m$  occurring through tilting of the  $SnI_6$  octahedra about the  $b$  axis. In contrast, no pressure-induced phase transformations are observed in the case of  $Cs_2SnCl_6$  and  $Cs_2SnBr_6$  crystals for applied pressures of up to about 12 GPa, which originates from the lower polarizability of chlorine and bromine relative to iodine atoms. The results are supported by DFT calculations, which also predict the thermodynamic stability of the FCC structure for  $Cs_2SnCl_6$  and  $Cs_2SnBr_6$  at the above pressure range. On the other hand, DFT results for  $Cs_2SnI_6$  show that the  $I2/m$  phase, with similar structural parameters to those deduced by SXRD, is the only metastable structure above 2 GPa and the lowest-energy phase above 4.7 GPa. Considering that introduction of local strains in the structure, e.g., by substitutional alloying, compensates for the imposed high pressure, our results provide key directions for modifying the local structure of the defect halide perovskites toward improving their optoelectronic properties and exploiting their use in photovoltaic applications.

#### ■ ASSOCIATED CONTENT

##### Supporting Information

The Supporting Information is available free of charge on the ACS Publications website at DOI: 10.1021/acs.jpcc.8b08449.

Lattice constants and shortest interatomic distances for FCC  $Cs_2SnI_6$  at various pressures (Table S1); values of zero-pressure Raman frequencies, frequency shift vs pressure slopes, and reduced slopes for  $Cs_2SnI_6$  at the  $I2/m$  phase (Table S2); plots of FWHM of the FCC (222) reflection vs pressure for  $Cs_2SnBr_6$  and  $Cs_2SnI_6$  (Figure S1a,b); experimental and simulated XRD patterns for  $Cs_2SnI_6$  at 0.29 GPa (FCC phase) and 10.9 GPa ( $I2/m$  phase) (Figure S2a,b); average inter- and intra-octahedral I–I distances for  $\alpha$ - $Cs_2SnI_6$  based on Rietveld refinements (Figure S3); plot of intensity of the Raman modes #3 and #4 normalized to that of band #2 vs pressure in  $Cs_2SnI_6$  (Figure S4); analysis of the Raman frequency shifts in  $Cs_2SnI_6$  for a 1 bar–19 GPa–

1 bar pressure cycle (Figure S5); sequential background corrected Raman spectra upon increasing–decreasing pressure cycle in  $\text{Cs}_2\text{SnBr}_6$  and  $\text{Cs}_2\text{SnCl}_6$  (Figure S6a,b); distance between Sn atoms and their iodine neighbors in the  $\beta$ -phase of  $\text{Cs}_2\text{SnI}_6$  as a function of applied pressure based on DFT calculations (Figure S7); difference in enthalpy between the  $\alpha$ - and  $\beta$ -phases of  $\text{Cs}_2\text{SnBr}_6$  and  $\text{Cs}_2\text{SnCl}_6$  as a function of pressure based on DFT calculations (Figure S8) (PDF)

## AUTHOR INFORMATION

### Corresponding Author

\*E-mail: [a.kontos@inn.demokritos.gr](mailto:a.kontos@inn.demokritos.gr). Tel: +30 2106503668. Fax: +30 2106511766.

### ORCID

Athanassios G. Kontos: 0000-0001-9193-0198

Constantinos C. Stoumpos: 0000-0001-8396-9578

Andreas Kaltzoglou: 0000-0002-3093-9778

Xiaofeng Guo: 0000-0003-3129-493X

Mercouri G. Kanatzidis: 0000-0003-2037-4168

Polycarpos Falaras: 0000-0002-9553-5301

### Author Contributions

#G.B. and M.K. contributed equally to this work.

### Notes

The authors declare no competing financial interest.

## ACKNOWLEDGMENTS

A.G.K. and P.F. acknowledge financial support from European Union's Horizon 2020 research and innovation program under the Marie Skłodowska-Curie grant agreement No 764787 (MAESTRO ITN project). X.L. acknowledges the support from NSFC Grant Nos. U1530402 and 17N1041. CHESS is supported by the NSF award DMR-1332208. M.G.K. was supported by the Department of Energy, Office of Science, Basic Energy Sciences, under Grant SC0012541 (synthesis, SXRD and physical characterization). The calculations used resources of the national HPC facility—ARIS—at the Greek Research & Technology Network (GRNET) under project pr004034-STEM.

## REFERENCES

- (1) Stranks, S. D.; Snaith, H. J. Metal-halide Perovskites for Photovoltaic and Light-emitting Devices. *Nat. Nanotechnol.* **2015**, *10*, 391–402.
- (2) Gao, P.; Grätzel, M.; Nazeeruddin, M. K. Organohalide Lead Perovskites for Photovoltaic Applications. *Energy Environ. Sci.* **2014**, *7*, 2448–2463.
- (3) Wang, F.; Ma, J.; Xie, F.; Li, L.; Chen, J.; Fan, J.; Zhao, N. Organic Cation-Dependent Degradation Mechanism of Organotin Halide Perovskites. *Adv. Funct. Mater.* **2016**, *26*, 3417–3423.
- (4) Lee, B.; Stoumpos, C. C.; Zhou, N.; Hao, F.; Malliakas, C.; Yeh, C.-Y.; Marks, T. J.; Kanatzidis, M. G.; Chang, R. P. H. Air-Stable Molecular Semiconducting Iodosalts for Solar Cell Applications:  $\text{Cs}_2\text{SnI}_6$  as a Hole Conductor. *J. Am. Chem. Soc.* **2014**, *136*, 15379–15385.
- (5) Xiao, Z.; Zhou, Y.; Hosono, H.; Kamiya, T. Intrinsic Defects in a Photovoltaic Perovskite Variant  $\text{Cs}_2\text{SnI}_6$ . *Phys. Chem. Chem. Phys.* **2015**, *17*, 18900–18903.
- (6) Kafil, G.; Ohta, T.; Koyanagi, T.; Vigneshwaran, M.; Zhang, Y.; Ogomi, Y.; Pandey, S. S.; Yoshino, K.; Shen, Q.; Toyoda, T.; et al. Investigation of Interfacial Charge Transfer in Solution Processed  $\text{Cs}_2\text{SnI}_6$  Thin Films. *J. Phys. Chem. C* **2017**, *121*, 13092–13100.

(7) Maughan, A. E.; Ganose, A. M.; Bordelon, M. M.; Miller, E. M.; Scanlon, D. O.; Neilson, J. R. Defect Tolerance to Intolerance in the Vacancy-Ordered Double Perovskite Semiconductors  $\text{Cs}_2\text{SnI}_6$  and  $\text{Cs}_2\text{TeI}_6$ . *J. Am. Chem. Soc.* **2016**, *138*, 8453–8464.

(8) Ke, J. C.-R.; Lewis, D. J.; Walton, A. S.; Spencer, B. F.; O'Brien, P.; Thomas, A. G.; Flavell, W. R. Ambient-air-stable Inorganic  $\text{Cs}_2\text{SnI}_6$  Double Perovskite Thin Films via Aerosol-assisted Chemical Vapour Deposition. *J. Mater. Chem. A* **2018**, *6*, 11205–11214.

(9) Qiu, X.; Cao, B.; Yuan, S.; Chen, X.; Qiu, Z.; Jiang, Y.; Ye, Q.; Wang, H.; Zeng, H.; Liu, J.; et al. From Unstable  $\text{CsSnI}_3$  to Air-stable  $\text{Cs}_2\text{SnI}_6$ : A Lead-free Perovskite Solar Cell Light Absorber with Band Gap of 1.48 eV and High Absorption Coefficient. *Sol. Energy Mater. Sol. Cells* **2017**, *159*, 227–234.

(10) Kaltzoglou, A.; Antoniadou, M.; Kontos, A. G.; Stoumpos, C. C.; Perganti, D.; Siranidi, E.; Raptis, V.; Trohidou, K.; Psycharis, V.; Kanatzidis, M. G.; et al. Optical-Vibrational Properties of the  $\text{Cs}_2\text{SnX}_6$  (X = Cl, Br, I) Defect Perovskites and Hole-Transport Efficiency in Dye-Sensitized Solar Cells. *J. Phys. Chem. C* **2016**, *120*, 11777–11785.

(11) Saparov, B.; Sun, J.-P.; Meng, W.; Xiao, Z.; Duan, H.-S.; Gunawan, O.; Shin, D.; Hill, I. G.; Yan, Y.; Mitzi, D. B. Thin-Film Deposition and Characterization of a Sn-Deficient Perovskite Derivative  $\text{Cs}_2\text{SnI}_6$ . *Chem. Mater.* **2016**, *28*, 2315–2322.

(12) Kaltzoglou, A.; Antoniadou, M.; Perganti, D.; Siranidi, E.; Raptis, V.; Trohidou, K.; Psycharis, V.; Kontos, A. G.; Falaras, P. Mixed-halide  $\text{Cs}_2\text{SnI}_3\text{Br}_3$  Perovskite as Low Resistance Hole-transporting Material in Dye-sensitized Solar Cells. *Electrochim. Acta* **2015**, *184*, 466–474.

(13) Jaffe, A.; Lin, Y.; Beavers, C. M.; Voss, J.; Mao, W. L.; Karunadasa, H. I. High-Pressure Single-Crystal Structures of 3D Lead-Halide Hybrid Perovskites and Pressure Effects on Their Electronic and Optical Properties. *ACS Cent. Sci.* **2016**, *2*, 201–209.

(14) Wang, L.; Wang, K.; Zou, B. Pressure-Induced Structural and Optical Properties of Organometal Halide Perovskite Based Formamidinium Lead Bromide. *J. Phys. Chem. Lett.* **2016**, *7*, 2556–2562.

(15) Ou, T.; Yan, J.; Xiao, C.; Shen, W.; Liu, C.; Liu, X.; Han, Y.; Ma, Y.; Gao, C. Visible Light Response, Electrical Transport, and Amorphization in Compressed Organolead Iodine Perovskites. *Nanoscale* **2016**, *8*, 11426–11431.

(16) Wang, Y.; Lu, X.; Yang, W.; Wen, T.; Yang, L.; Ren, X.; Wang, L.; Lin, Z.; Zhao, Y. Pressure-Induced Phase Transformation, Reversible Amorphization and Anomalous Visible Light Response in Organolead Bromide Perovskite. *J. Am. Chem. Soc.* **2015**, *137*, 11144–11149.

(17) Wang, L.; Wang, K.; Xiao, G.; Zeng, Q. C.; Zou, B. Pressure-Induced Structural Evolution and Band Gap Shifts of Organometal Halide Perovskite-Based Methylammonium Lead Chloride. *J. Phys. Chem. Lett.* **2016**, *7*, 5273–5279.

(18) Jaffe, A.; Lin, Y.; Karunadasa, H. I. Halide Perovskites under Pressure: Accessing New Properties through Lattice Compression. *ACS Energy Lett.* **2017**, *2*, 1549–1555.

(19) Tan, J. C.; Cheetham, A. K. Mechanical Properties of Hybrid Inorganic-organic Framework Materials: Establishing Fundamental Structure-property Relationships. *Chem. Soc. Rev.* **2011**, *40*, 1059–1080.

(20) Jiang, S.; Fang, Y.; Li, R.; Xiao, H.; Crowley, J.; Wang, C.; White, T. J.; Goddard, W. A.; Wang, Z.; et al. Pressure-Dependent Polymorphism and Band-Gap Tuning of Methylammonium Lead Iodide Perovskite. *Angew. Chem.* **2016**, *128*, 6650–6654.

(21) Lee, Y.; Mitzi, D. B.; Barnes, P. W.; Vogt, T. Pressure-induced Phase Transitions and Templating Effect in Three-dimensional Organic-inorganic Hybrid Perovskites. *Phys. Rev. B* **2003**, *68*, No. 020103(R).

(22) Lü, X.; Wang, Y.; Stoumpos, C. C.; Hu, Q.; Guo, X.; Chen, H.; Yang, L.; Smith, J. S.; Yang, W.; Zhao, Y.; et al. Enhanced Structural Stability and Photo Responsiveness of  $\text{CH}_3\text{NH}_3\text{SnI}_3$  Perovskite via Pressure-Induced Amorphization and Recrystallization. *Adv. Mater.* **2016**, *28*, 8663–8668.

- (23) Cai, Y.; Xie, W.; Ding, H.; Chen, Y.; Thirumal, K.; Wong, L. H.; Mathews, N.; Mhaisalkar, S. G.; Sherburne, M.; Asta, M. Computational Study of Halide Perovskite-Derived  $A_2BX_6$  Inorganic Compounds: Chemical Trends in Electronic Structure and Structural Stability. *Chem. Mater.* **2017**, *29*, 7740–7749.
- (24) Berg, R. W. Low Temperature Vibrational Spectroscopy. II. Evidence for Order–disorder Phase Transitions due to Weak C–H...Cl Hydrogen Bonding in Tetramethylammonium Hexachloroplatinate (IV), -Tellurate (IV), and -Stannate (IV) and the Related Perdeuterated Compounds. *J. Chem. Phys.* **1978**, *69*, 1325–1335.
- (25) Brendel, W.; Samartzis, T.; Brendel, C.; Krebs, B. TG and DTA Investigations on Hexaiodometallates. *Thermochim. Acta* **1985**, *83*, 167–172.
- (26) Shi, J. R.; Kume, Y.; Pelzl, J.; Xu, Y. C.; Wu, X. A Phase Transition in  $(CH_3NH_3)_2SnCl_6$  Investigated by Raman Scattering. *J. Raman Spectrosc.* **1998**, *29*, 149–151.
- (27) Pelzl, J.; Engels, P.; Florian, R. Raman Spectroscopic Study of the Structural Phase Transitions in  $K_2SnCl_6$ . *Phys. Status Solidi B* **1977**, *82*, 145–148.
- (28) Adams, D. M.; Berg, R. W.; Williams, A. D. Vibrational Spectroscopy at Very High Pressures. Part 28. Raman and Far-infrared Spectra of Some Complex Chlorides  $A_2MCl_6$  Under Hydrostatic Pressure. *J. Chem. Phys.* **1981**, *74*, 2800–2807.
- (29) Yuan, G.; Huang, S.; Niu, J.; Qin, S.; Wu, X.; Ding, H.; Lu, A. Compressibility of  $Cs_2SnBr_6$  by X-ray Diffraction and Raman Spectroscopy. *Solid State Commun.* **2018**, *275*, 68–72.
- (30) Schülpp, B.; Heines, P.; Savin, A.; Keller, H.-L. Crystal Structures and Pressure-Induced Redox Reaction of  $Cs_2Pdl_4I_2$  to  $Cs_2Pdl_6$ . *Inorg. Chem.* **2000**, *39*, 732–735.
- (31) Heines, P.; Keller, H.-L.; Armbruster, M.; Schwarz, U.; Tse, J. Pressure-Induced Internal Redox Reaction of  $Cs_2[PdI_4] I_2$ ,  $Cs_2[PdBr_4] I_2$ , and  $Cs_2[PdCl_4] I_2$ . *Inorg. Chem.* **2006**, *45*, 9818–9825.
- (32) Maughan, A. E.; Ganose, A. M.; Almaker, M. A.; Scanlon, D. O.; Neilson, J. R. Tolerance Factor and Cooperative Tilting Effects in Vacancy-Ordered Double Perovskite Halides. *Chem. Mater.* **2018**, *30*, 3909–3919.
- (33) Forman, R. A.; Piermarini, G. J.; Barnett, J. D.; Block, S. Pressure Measurement Made by the Utilization of Ruby Sharp-Line Luminescence. *Science* **1972**, *176*, 284–285.
- (34) Hammersley, A. P. FIT2D: A Multi-purpose Data Reduction, Analysis and Visualization Program. *J. Appl. Crystallogr.* **2016**, *49*, 646–652.
- (35) Petříček, V.; Dušek, M.; Palatinus, L. Crystallographic Computing System JANA2006: General Features. *Z. Kristallogr. – Cryst. Mater.* **2014**, *229*, 345–352.
- (36) Howard, C. J.; Kennedy, B. J.; Woodward, P. M. Ordered Double Perovskites - A Group-theoretical Analysis. *Acta Crystallogr., Sect. B: Struct. Sci.* **2003**, *59*, 463–471.
- (37) Roisnel, T.; Rodriguez-Carvajal, J. *FULLPROF: A Program for Rietveld Refinement and Pattern Matching Analysis*, version Sept. 2012, France.
- (38) Tiginyanu, I. M.; Ursaki, V. V.; Raptis, Y. S.; Stergiou, V.; Anastassakis, E.; Hartnagel, H. L.; Vogt, A.; Prévot, B.; Schwab, C. Raman Modes in Porous GaP Under Hydrostatic Pressure. *Phys. Stat. Sol. (b)* **1999**, *211*, 281–286.
- (39) Giannozzi, P.; Baroni, S.; Bonini, N.; Calandra, M.; Car, R.; Cavazzoni, C.; Ceresoli, D.; Chiarotti, G. L.; Cococcioni, M.; Dabo, I.; et al. QUANTUM ESPRESSO: A Modular and Open-source Software Project for Quantum Simulations of Materials. *J. Phys.: Condens. Matter* **2009**, *21*, No. 395502.
- (40) Blöchl, P. E. Projector Augmented-wave Method. *Phys. Rev. B* **1994**, *50*, 17953.
- (41) Kresse, G.; Joubert, D. From Ultrasoft Pseudopotentials to the Projector Augmented-wave Method. *Phys. Rev. B* **1999**, *59*, 1758.
- (42) Perdew, J. P.; Wang, Y. Accurate and Simple Analytic Representation of the Electron-gas Correlation Energy. *Phys. Rev. B* **1992**, *45*, 13244.
- (43) Grimme, S. Semiempirical GGA-type Density Functional Constructed with a Long-range Dispersion Correction. *J. Comput. Chem.* **2006**, *27*, 1787–1799.
- (44) Chung, I.; Song, J.-H.; Im, J.; Androulakis, J.; Malliakas, C. D.; Li, H.; Freeman, A. J.; Kenney, J. T.; Kanatzidis, M. G.  $CsSnI_3$ : Semiconductor or Metal? High Electrical Conductivity and Strong Near-Infrared Photoluminescence from a Single Material. High Hole Mobility and Phase-Transitions. *J. Am. Chem. Soc.* **2012**, *134*, 8579–8587.
- (45) Lee, B.; Stoumpos, C. C.; Zhou, N.; Hao, F.; Malliakas, C.; Yeh, C. Y.; Marks, T. J.; Kanatzidis, M. G.; Chang, R. P. H. Air-Stable Molecular Semiconducting Iodosalts for Solar Cell Applications:  $Cs_2SnI_6$  as a Hole Conductor. *J. Am. Chem. Soc.* **2014**, *136*, 15379–15385.
- (46) Chadi, D. J.; Cohen, M. L. Special Points in the Brillouin Zone. *Phys. Rev. B* **1973**, *8*, 5747.
- (47) Birch, F. Finite Elastic Strain of Cubic Crystals. *Phys. Rev.* **1947**, *71*, 809.
- (48) Murnaghan, F. D. The Compressibility of Media Under Extreme Pressures. *Proc. Natl. Acad. Sci. U.S.A.* **1944**, *30*, 244–247.
- (49) Lü, X.; Yang, W.; Jia, Q.; Xu, H. Pressure-induced Dramatic Changes in Organic–Inorganic Halide Perovskites. *Chem. Sci.* **2017**, *8*, 6764–6776.
- (50) Fuchizaki, K.; Hamaya, N. Equation of State for the Low-pressure Crystalline Phase of  $SnI_4$ . *Phys. Rev. B* **2011**, *84*, No. 144105.
- (51) Shannon, R. D. Revised Effective Ionic Radii and Systematic Studies of Interatomic Distances in Halides and Chalcogenides. *Acta Crystallogr., Sect. A: Found. Adv.* **1976**, *32*, 751–767.
- (52) Lekgoathi, M. D. S.; Kock, L. D. Effect of Short and Long Range Order on Crystal Structure Interpretation: Raman and Powder X-ray Diffraction of  $LiPF_6$ . *Spectrochim. Acta, Part A* **2016**, *153*, 651–654.
- (53) Boysen, H.; Ihringer, J.; Prandl, W.; Yelon, W. X-Ray and Neutron Investigations of the Phase Instabilities in  $K_2SnCl_6$ . *Solid State Commun.* **1976**, *20*, 1019–1024.
- (54) Yafe, O.; Guo, Y.; Tan, L. Z.; Egger, D. A.; Hull, T.; Stoumpos, C. C.; Zheng, F.; Heinz, T. F.; Kronik, L.; Kanatzidis, M. G.; et al. Local Polar Fluctuations in Lead Halide Perovskite Crystals. *Phys. Rev. Lett.* **2017**, *118*, No. 136001.
- (55) Kroumova, E.; Aroyo, M. I.; Perez-Mato, J. M.; Kirov, A.; Capillas, C.; Ivantchev, S.; Wondratschek, H. Bilbao Crystallographic Server: Useful Databases and Tools for Phase-Transition Studies. *Phase Transitions* **2003**, *76*, 155–170.
- (56) Huang, H.-M.; Jiang, Z.-Y.; Luo, S.-J. First Principles Investigations on the Mechanical, Thermal, Electronic, and Optical Properties of the Defect Perovskites  $Cs_2SnX_6$  ( $X = Cl, Br, I$ ). *Chin. Phys. B* **2017**, *26*, No. 096301.
- (57) Hochheimer, H. D.; Kuchta, B.; Dorhout, P. K.; Yarger, J. L., Eds. *Frontiers of High Pressure Research II: Application of High Pressure to Low-Dimensional Novel Electronic Materials*; Nato Science Series II; Springer, 2001; Vol. 48.
- (58) Brik, M. G.; Kityk, I. V. Modeling of Lattice Constant and Their Relations with Ionic Radii and Electronegativity of Constituting Ions of  $A_2XY_6$  Cubic Crystals ( $A = K, Cs, Rb, Tl$ ;  $X =$  tetravalent cation,  $Y = F, Cl, Br, I$ ). *J. Phys. Chem. Solids* **2011**, *72*, 1256–1260.